Self-Similar Propagation and Compression of the Parabolic Pulse in Silicon Waveguide

Chao Mei, Kuiru Wang, Jinhui Yuan, *Senior Member*, *IEEE*, *Senior Member*, *OSA*, Zhe Kang, Xianting Zhang, Binbin Yan, Xinzhu Sang, Qiang Wu, Xian Zhou, Chongxiu Yu, and Gerald Farrell

***Abstract*—In this paper, the conditions of the self-similar propagation of the parabolic pulse (PP) in passive nonlinear tapers are derived and classified into the three cases. Analytical solutions of the inhomogeneous nonlinear Schrödinger equation (INLSE) for the three cases are obtained. Numerical verifications of these analytical solutions are demonstrated by designing the silicon waveguide tapers. Moreover, we further design three kinds of cascaded silicon waveguides for realizing the PP generation and compression. The PP compression occurs at the anomalous-dispersion segment of the cascaded silicon waveguide. The generalized INLSE is used to model the generation and compression of the PP. When considering the higher-order dispersion, higher-order nonlinearity, and losses, the complex nonlinear dynamics are investigated. Simulation results show that a 300-fs Gaussian input pulse can evolve to the PP and be compressed to 35.6-fs in the cascaded silicon waveguide.**

***Index Terms*—Self-similar propagation, parabolic pulse, nonlinear silicon photonics.**

I. INTRODUCTION

PARABOLIC pulse (PP) has attracted great attention since it was reported in 1993 [1]. Up to now, the PP has been investigated in optical amplifiers [2, 3], fiber lasers [4, 5], and optical communications [6-10]. The dynamics of the PP generations in the group-velocity dispersion (GVD)-decreasing fiber taper and silicon waveguide taper have also been analyzed [11,12]. Theoretical models for the PP generation in the active and passive nonlinear media are demonstrated [13]. These models describe several cases on the PP generation, where the PP with a linear chirp can be compressed in media with anomalous GVD profile.

Generally speaking, pulse compression can be achieved by the two nonlinear compression techniques including soliton compression and non-soliton compression [14, 15]. Soliton compression was demonstrated in optical fiber [16] and silicon waveguide taper [17, 18], chalcogenide-silicon slot waveguide taper [19], silicon photonic crystal waveguide [20], and GaInP photonic crystal waveguide [21]. Non-soliton compression was reported in dispersive fiber [22], fiber grating [23], and hollow-core fiber [24]. Recently, non-soliton compression has been realized in silicon chirper [25, 26], which provides a promising solution to realize on-chip pulse source. The PP compression as non-soliton compression can be achieved by negative-slope chirp compensation, and the transformed-limit pulse could be obtained. At present, the on-chip PP compression has not been reported yet. In order to better show the generation and compression scheme of the PP in passive waveguide, a conceptual diagram is shown in Fig. 1. From Fig. 1, the input pulse with an arbitrary waveform can evolve into the PP after a nonlinear taper. The PP generated has a linear

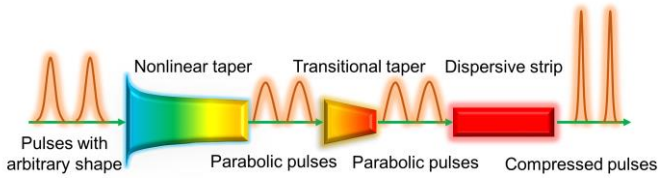

Fig. 1. Conceptual diagram of passive generation and compression of the PP.

chirp with positive slope and remains unchanged after passing through the transitional taper. The role of the transitional taper is to transform the GVD from the normal to anomalous region. Finally, the PP is compressed when it propagates inside the dispersive strip with anomalous dispersion profile.

The paper is arranged as follows. In section II, the condition of self-similar propagation of the PP in passive nonlinear taper is derived and classified into the three cases. The analytical solutions of inhomogeneous nonlinear Schrödinger equation (INLSE) are obtained. After that, three kinds of silicon waveguide tapers are designed, and analytical solutions of INLSE are numerically verified. In section III, three kinds of cascaded silicon waveguides based on the silicon waveguide taper are proposed for the PP generation and compression. The generalized INLSE (GINLSE) is used to model the nonlinear propagation dynamics of the PP. In section IV, the conclusions

Supported by the National Natural Science Foundation of China (61875238 and 61475023), Beijing Youth Top-notch Talent Support Program (2015000026833ZK08), BUPT Excellent Ph.D. Students Foundation (CX2017316), Fund of State Key Laboratory of Information Photonics and Optical Communications (BUPT) P. R. China (IPOC2017ZZ05), Shenzhen Science and Technology Innovation Commission (JCYJ20160331141313917), and the Research Grant Council of the Hong Kong S.A.R. of China (PolyU152144/15E). (The corresponding author is Jinhui Yuan, e-mail: yuanjinhui81@bupt.edu.cn).

Chao Mei, Kuiru Wang, Jinhui Yuan, Xinzhu Sang, Binbin Yan, and Chongxiu Yu are with the State Key Laboratory of Information Photonics and Optical Communications, Beijing University of Posts and Telecommunications, Beijing, P. R. China.

Jinhui Yuan, Zhe Kang, Xianting Zhang, and Xian Zhou are with the Photonics Research Centre, Department of Electronic and Information Engineering, the Hong Kong Polytechnic University, Hung Hom, Hong Kong S. A. R., P. R. China.

Jinhui Yuan is also with the Hong Kong Polytechnic University Shenzhen Research Institute, Shenzhen, P. R. China.

Qiang Wu is with the Department of Physics and Electrical Engineering, Northumbria University, Newcastle upon Tyne, NE1 8ST, United Kingdom.

Gerald Farrell is with Photonics Research Centre, Dublin Institute of Technology, Dublin, Ireland.

are drawn.

II. Analytical Investigation Of the Self-similar Propagation

The nonlinear dynamics of the pulse propagation in a passive nonlinear taper can be modeled by the INLSE with linear loss as following [13]

$$\frac{\partial A}{\partial z}=-\frac{i\beta_0\theta(z)}{2}\frac{\partial^2 A}{\partial t^2}+i\gamma_0\varepsilon(z)\left|A\right|^2A-\frac{\alpha_1(z)}{2}A, \quad (1)$$

where $A(z, t)$ is the carrier envelop of slow-varying electric field, z is the propagation distance, t is the retarded time, β_0 is the initial value of $\beta_2(z)$ at $z = 0$, $\theta(z)$ is the normalized function describing the variation of GVD and $\theta(0) = 1$, γ_0 is the initial value of nonlinear coefficient $\gamma(z)$ at $z = 0$, $\varepsilon(z)$ is the normalized function describing the variation of nonlinearity and $\varepsilon(0) = 1$, and $\alpha_l(z) > 0$ represents the linear loss. $\gamma(z)$ and $\beta_2(z)$ can be written as

$$\gamma(z)=\gamma_0\varepsilon(z), \qquad \beta_2(z)=\beta_0\theta(z). \quad (2)$$

In the normal GVD region, $\beta_0 > 0$ and $\theta(z) > 0$. $\kappa(z)$ is defined as

$$\kappa(z)=\int_0^z\theta(z')dz'. \quad (3)$$

If $\kappa(z)$ is a monotonic function, its inverse $z(\kappa)$ should exist. Thus Eq. (1) can be written as

$$\frac{\partial A}{\partial \kappa}=-\frac{i\beta_0}{2}\frac{\partial^2 A}{\partial t^2}+i\gamma_0\frac{\bar{\varepsilon}(\kappa)}{\bar{\theta}(\kappa)}\left|A\right|^2A-\frac{\bar{\alpha}_1(\kappa)}{2\bar{\theta}(\kappa)}A. \quad (4)$$

The amplitude $A(z, t)$ is redefined as

$$A=a(\kappa)u(\kappa,t), \quad (5)$$

where u is a new amplitude function in κ space and can be obtained from A which is divided by a given function $a(\kappa)$. Substituting Eq. (5) into Eq. (4), we have

$$\frac{\partial u}{\partial \kappa}=-\frac{i\beta_0}{2}\frac{\partial^2 u}{\partial t^2}+i\gamma_0\frac{a^2(\kappa)\bar{\varepsilon}(\kappa)}{\bar{\theta}(\kappa)}\left|u\right|^2u-\frac{\bar{\alpha}_1(\kappa)}{2\bar{\theta}(\kappa)}u-\frac{a'(\kappa)}{a(\kappa)}u. \quad (6)$$

To obtain the self-similar solution, Eq. (6) needs to be simplified to similar form with homogeneous nonlinear Schrödinger equation including constant gain [27], and the following two equations should be satisfied as

$$\frac{a^2(\kappa)\bar{\varepsilon}(\kappa)}{\bar{\theta}(\kappa)}=1, \quad (7)$$

$$-\frac{\bar{\alpha}_1(\kappa)}{2\bar{\theta}(\kappa)}-\frac{a'(\kappa)}{a(\kappa)}=\frac{g_{eq}}{2}, \quad (8)$$

where g_{eq} is a given parameter called equivalent gain. For the passive nonlinear taper, g_{eq} must be a constant and larger than zero. By solving Eq. (8), we can obtain

$$a(\kappa)=\exp\left[-\frac{g_{eq}\kappa}{2}-\frac{\alpha_1(\kappa)}{2}\int_0^\kappa\frac{1}{\bar{\theta}(\kappa')}d\kappa'\right]. \quad (9)$$

Substituting Eq. (7) into Eq. (9),

$$\bar{\varepsilon}(\kappa)=\bar{\theta}(\kappa)\exp\left(g_{eq}\kappa+\alpha_1(\kappa)\int_0^\kappa\frac{1}{\bar{\theta}(\kappa')}d\kappa'\right). \quad (10)$$

Return Eq. (10) from κ space to z space, we can obtain

$$\varepsilon(z)=\theta(z)\exp\left(g_{eq}\int_0^z\theta(z')dz'+\int_0^z\alpha_1(z')dz'\right). \quad (11)$$

According to Eq. (2) and Eq. (11), the relation between $\gamma(z)$ and $\beta_2(z)$ can be written as

$$\gamma(z)=\frac{\gamma_0\beta_2(z)}{\beta_0}\exp\left(\frac{g_{eq}}{\beta_0}\int_0^z\beta_2(z')dz'+\int_0^z\alpha_1(z')dz'\right). \quad (12)$$

Eq. (12) gives the condition that $\gamma(z)$ of the passive nonlinear taper must be satisfied for the self-similar propagation of the PP. The expressions of $\gamma(z)$, $\beta_2(z)$, and $\alpha_l(z)$ in Eq. (12) partially determine the solution of Eq. (1). In practice, compared to $\gamma(z)$ and $\beta_2(z)$, $\alpha_l(z)$ changes much less than $\gamma(z)$ and $\beta_2(z)$, thus it is regarded as a constant. To comprehensively understand Eq. (12), we classify it into three cases in the following discussions.

A. Variable $\gamma(z)$ and constant $\beta_2(z)$

For the Case 1, we consider that $\gamma(z)$ is variable and $\beta_2(z)$ is a constant. In this case, $\beta_2(z)=\beta_0$ and $\theta(z) = 1$, and Eq. (12) can be simplified as

$$\gamma(z)=\gamma_0\exp\left[\left(g_{eq}+\alpha_1\right)z\right]. \quad (13)$$

For the self-similar propagation of the PP, the high power component of the pulse broadens faster than the low power component of the pulse at the leading and trailing edges because of exponentially increasing $\gamma(z)$. The self-similar solution of the PP is given as

$$A(z,t)=\sqrt{P(z)}\left(1-t^2/t_p^2\right)^{1/2}\exp\left[i\varphi(z,t)\right], \quad (14)$$

where $P(z)$ is the peak power, $t_p(z)$ is the pulse width, and $\varphi(z, t)$ is the phase. The initial phase is assumed to be zero. When Eq. (13) is satisfied, Eq. (1) can be solved by the self-similar technique [13]. The peak power is obtained as

$$P(z)=\frac{\left(g_{eq}E_{in}\right)^{2/3}}{4}\left(\frac{2}{\gamma_0\beta_0}\right)^{1/3}\exp\left[-\left(\frac{1}{3}g_{eq}+\alpha_1\right)z\right]. \quad (15)$$

where E_{in} is the initial energy. It can be seen from Eq. 15 that $P(z)$ decreases exponentially with z. $t_p(z)$ and $\varphi(z, t)$ can be described as

$$t_p(z)=3\left(\frac{E_{in}\gamma_0\beta_0}{2g_{eq}^2}\right)^{1/3}\exp\left(\frac{1}{3}g_{eq}z\right). \quad (16)$$

$$\phi(z,t)=\frac{3}{8}\left(\frac{\gamma_0E_{in}}{\sqrt{g_{eq}\beta_0/2}}\right)^{2/3}\exp\left(\frac{2g_{eq}z}{3}\right)-\frac{g_{eq}}{6\beta_0}t^2. \quad (17)$$

Eq. (16) indicates that $t_p(z)$ increases exponentially with z. It should be noted that α_l has no influence on $t_p(z)$ and $\varphi(z, t)$ but only on $P(z)$. Besides, the linear chirp with a positive slope can be obtained from Eq. (17).

B. Constant $\gamma(z)$ and variable $\beta_2(z)$

For the Case 2, $\gamma(z)$ is constant and $\beta_2(z)$ is variable. In this case, $\gamma(z) = \gamma_0$ and $\varepsilon(z) = 1$. Eq. (11) can be rewritten as

$$\frac{1}{\theta(z)}=\exp\left(g_{eq}\int_0^z\theta(z')dz'+\alpha_1z\right). \quad (18)$$

By eliminating the integration at right-hand side of Eq. (18), a Bernoulli equation can be obtained as

$$-\theta'(z)=g_{eq}\theta^2(z)+\alpha_1\theta(z). \quad (19)$$

By solving Eq. (19), we can obtain the solution of $\theta(z)$ as

$$\theta(z)=\frac{\alpha_1}{\left(g_{\mathrm{eq}}+\alpha_1\right)\exp\left(\alpha_1 z\right)-g_{\mathrm{eq}}}. \quad (20)$$

Thus, $\beta_2(z)$ can be written as

$$\beta_2(z)=\frac{\alpha_1\beta_0}{\left(g_{\mathrm{eq}}+\alpha_1\right)\exp\left(\alpha_1 z\right)-g_{\mathrm{eq}}}. \quad (21)$$

At this time, $\beta_2(z)$ decreases as z increases, so the effect of the GVD becomes weaker than that of the nonlinearity. As a result, the high power component of the pulse broadens faster than the low power component of the pulse at the leading and trailing edges. Combining with Eq. (21), Eq. (1) can be solved by the means of self-similar technique. The form of self-similar solution of the PP is the same as Eq. (14), and $P(z)$ is derived as

$$P(z)=\frac{\left(g_{\mathrm{eq}}E_{\mathrm{in}}\right)^{2/3}}{4}\left[\frac{2\theta(z)}{\gamma_0\beta_0}\right]^{1/3}\exp\left(-\frac{2}{3}\alpha_1 z\right). \quad (22)$$

It can be seen from Eq. (22) that $P(z)$ is proportional to $\theta(z)$ and inversely proportional to α_1. $t_{\mathrm{p}}(z)$ and $\varphi(z, t)$ of the PP are obtained as

$$t_{\mathrm{p}}(z)=3\left[\frac{E_{\mathrm{in}}\gamma_0\beta_0}{2g_{\mathrm{eq}}^2\theta(z)}\right]^{1/3}\exp\left(-\frac{\alpha_1 z}{3}\right), \quad (23)$$

$$\varphi(z,t)=\frac{3}{8}\left[\frac{\sqrt{2}E_{\mathrm{in}}\gamma_0}{\theta(z)\sqrt{g_{\mathrm{eq}}\beta_0}}\right]^{2/3}\exp\left(-\frac{2\alpha_1 z}{3}\right)-\frac{g_{\mathrm{eq}}t^2}{6\beta_0}. \quad (24)$$

Here, $t_{\mathrm{p}}(z)$ and $\varphi(z, t)$ are related to α_1, which is different from that in the Case 1. Therefore, although the self-similar propagation of the PP can be theoretically achieved in the Case 1 and Case 2, nonlinear mechanisms behind them are different.

C. Variable $\gamma(z)$ and variable $\beta_2(z)$

For the Case 3, $\gamma(z)$ and $\beta_2(z)$ are changed simultaneously. The self-similar propagation of the PP is jointly determined by the normalized functions $\varepsilon(z)$ and $\theta(z)$. In this case, Eq. (12) can be written as

$$\gamma(z)=\frac{\gamma_0\beta_2(z)}{\beta_0}\exp\left(\frac{g_{\mathrm{eq}}}{\beta_0}\int_0^z\beta_2(z')dz'+\alpha_1 z\right), \quad (25)$$

$P(z)$ can be described as

$$P(z)=\frac{\left(g_{\mathrm{eq}}E_{\mathrm{in}}\right)^{2/3}}{4}\left(\frac{2}{\gamma_0\beta_0}\right)^{1/3}\frac{\theta(z)}{\varepsilon(z)}\exp\left[\frac{2}{3}g_{\mathrm{eq}}\int_0^z\theta(z')dz'\right]. \quad (26)$$

In Eq. (26), $P(z)$ is proportional to $\theta(z)$ and inversely proportional to $\varepsilon(z)$, so the evolution of $P(z)$ is determined by $\gamma(z)$ and $\beta_2(z)$. When $\gamma(z)$ and $\beta_2(z)$ satisfy Eq. (25), the PP can be kept unchanged during the propagation. Thus, $t_{\mathrm{p}}(z)$ and $\varphi(z, t)$ of the PP are derived as

$$t_{\mathrm{p}}(z)=3\left(\frac{E_{\mathrm{in}}\gamma_0\beta_0}{2g_{\mathrm{eq}}^2}\right)^{1/3}\frac{\varepsilon(z)}{\theta(z)}\exp\left[\frac{-2g_{\mathrm{eq}}}{3}\int_0^z\theta(z')dz'-\alpha_1 z\right]. \quad (27)$$

$$\varphi(z,t)=\frac{3}{8}\left(\frac{\sqrt{2}\gamma_0E_{\mathrm{in}}}{\sqrt{g_{\mathrm{eq}}\beta_0}}\right)^{2/3}\exp\left[\frac{2g_{\mathrm{eq}}}{3}\int_0^z\theta(z')dz'\right]-\frac{g_{\mathrm{eq}}t^2}{6\beta_0}. \quad (28)$$

It can be seen from Eq. (27) that α_1 only contributes to $t_{\mathrm{p}}(z)$. Similar to the Case 1 and Case 2, the chirp of the PP is independent on z and remains an constant, $g_{\mathrm{eq}}/(3\beta_0)$, during the whole propagation. From the above analyses, the self-similar propagation of the PP could be achieved theoretically for the three cases considered.

D. Numerical verification of the self-similar solution

According to the conditions of self-similar propagation for the Case 1, Case 2, and Case 3, three kinds of silicon waveguide tapers are designed. Because it is difficult to achieve that only $\gamma(z)$ or $\beta_2(z)$ is variable in one waveguide taper, the effective GVD and nonlinearity values are introduced in the Case 1 and Case 2 as following

$$\beta_{2,\mathrm{eff}}=\int_0^L\beta_2(z)dz\Big/L, \quad (29) \quad \text{and} \quad \gamma_{\mathrm{eff}}=\int_0^L\gamma(z)dz\Big/L. \quad (30)$$

where L is the length of silicon waveguide taper. α_1 is set to be 0.5 dB/cm. The widths W of the three silicon waveguide tapers at the input and output ports are 1600 and 800 nm, respectively. The height H is 220 nm. Fig. 2(a) shows the variation of the W along z for the three cases. The cross-section and corresponding three-dimensional (3D) view are shown in the Insets I and II, respectively. As seen from Insets I and II, the silicon waveguide taper is buried in the SiO_2 cladding, and the optical field energy can be well confined within the waveguide taper when pump wavelength is located at 1550 nm. The relationships between γ, β_2 and z can be obtained from Eq. (13) and Eq. (21) for the Case 1 and Case 2, and the bisection method is used to solve Eqs. (25) for obtaining $\gamma(z)$ and $\beta_2(z)$ for the Case 3. Fig. 2(b) shows $\gamma(z)$, $\beta_2(z)$, and $\beta_{2,\mathrm{eff}}$ along z for the Case 1. $\beta_{2,\mathrm{eff}}$ is calculated as 1.13 $\times10^{-24}$ ps^2/m. In Fig. 1(c), $\gamma(z)$, $\beta_2(z)$, and γ_{eff} are plotted for the Case 2, where γ_{eff} is 119.89 W^{-1}m^{-2}. In Fig. 2(d), $\gamma(z)$ and $\beta_2(z)$ are shown for the Case 3, and no effective value is needed. It can be seen from Figs. 2(b), 2(c), and 2(d) that $\gamma(z)$ increases while $\beta_2(z)$ decreases along z for the three cases.

In the following, the 4-th order Runge-Kutta method is used to numerically solve Eq. (1). For the Case 1, the calculation results are shown in Fig. 3, where the black solid curves represent the numerical powers under $\beta_{2,\mathrm{eff}}$ and red dashed curves correspond to their parabolic fittings at z = 0, 0.2, 0.4, 0.6, 0.8, and 1 cm. We can see that the numerical powers under $\beta_{2,\mathrm{eff}}$ can be well fitted. Besides, the analytical chirp obtained from Eq. (17) is also plotted in Fig. 3, which agrees well with the numerical chirp in the cyan region. The propagation pulse keeps its parabolic profile unchanged. Thus, the condition of self-similar propagation for the Case 1 is verified. During the propagation of the pulse, the effect of GVD is gradually reduced. As a result, the speed of the pulse stretching is reduced. However, due to the nonlinearity, new frequency components are generated at long and short wavelengths, corresponding to the leading and trailing edges of the temporal pulse. At this time, new frequency components propagate more slowly than the original frequency components which are located at the high power portion of the pulse in the time domain. Thus, the middle part of pulse begins to swell. The specific shape after the pulse expansion is determined by the variations of the GVD coefficient, nonlinear coefficient, and linear loss. In this work, the waveguide is designed for the PP propagation. When $\beta_2(z)$ is used in the numerical simulation instead of $\beta_{2,\mathrm{eff}}$, the output

numerical powers are nearly accordant with that under $\beta_{2,\text{eff}}$, and the maximum power difference is only 0.02 W over the propagation, as shown in Fig. 3. Also, the numerical chirps

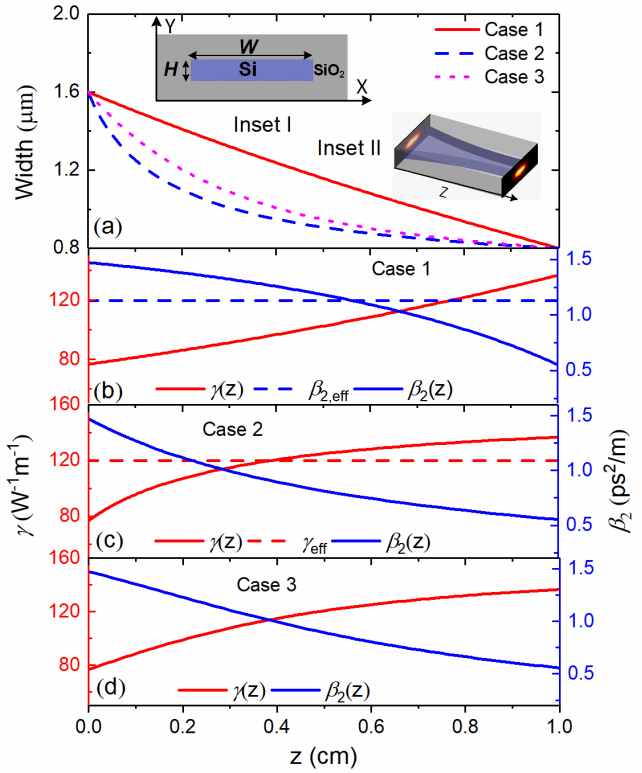

Fig. 2. (a) Waveguide width versus z for the Case 1 (red solid curve), Case 2 (blue dashed curve), and Case 3 (pink dot curve), the insets I and II showing the cross-section and 3D view of the proposed silicon waveguide taper along with optical field distributions. Nonlinear coefficient $\gamma(z)$ (red solid curve), GVD $\beta_2(z)$ (blue solid curve) for (b) Case 1, (c) Case 2, and (d) Case 3. Effective $\beta_2(z)$ (blue dashed curve) and $\gamma(z)$ (red dashed curve) are also shown in (b) and (c), respectively.

under $\beta_2(z)$ is almost the same as that under $\beta_{2,\text{eff}}$ along with maximum difference of 0.41 THz in the cyan region. The differences are very small. Since $\beta_2(z)$ decreases with z, the effect of GVD is further weakened. But the balance between the nonlinear and GVD can still be maintained. Therefore, for the Case 1, the silicon waveguide taper designed can support the self-similar propagation of the PP, and $\beta_{2,\text{eff}}$ used is reasonable.

Fig. 4 shows the propagation of the PP calculated for the Case 2, where the black solid curves and red dashed curves correspond to the numerical powers and parabolic fittings at z = 0, 0.2, 0.4, 0.6, 0.8, and 1 cm, respectively. The pulse shape is kept as the parabolic profile and numerical chirps coincide well with the analytical ones in the cyan region. The self-similar propagation of the PP is observed, so the condition of self-similar propagation of the PP is valid. For the Case 2, the self-similar propagation of the PP is different from that shown in Fig. 2. The effects of GVD and nonlinearity are simultaneously weakened, which leads to the reduction of the

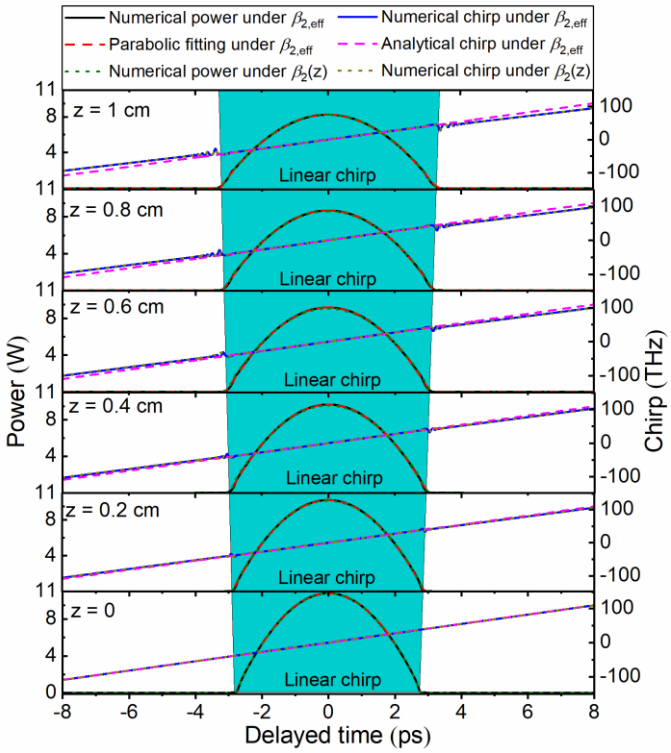

Fig. 3. The powers and chirps of the PP propagation in the designed silicon waveguide taper for the Case 1. Numerical powers (black solid curve) and chirps (blue solid curve), parabolic fittings (red dashed curve) and analytical chirps (pink dashed curve) under $\beta_{2,\text{eff}}$, numerical powers (olive dot curve) and chirps (dark yellow dot curve) under $\beta_2(z)$ are shown at z = 0, 0.2, 0.4, 0.6, 0.8, and 1 cm, respectively. The cyan region corresponds to the region of the linear chirp.

new frequency components. At this time, the GVD coefficient is a variable that decreases as z increases, and the effect of GVD becomes weaker than that in the Case 1. The simultaneously reduced effects of the nonlinearity and GVD reach a new balance. Therefore, self-similar propagation can still occur. It is conceivable that self-similar propagation in this case is more difficult to achieve than the Case 1 due to the weak interaction. Thus, higher peak power is needed. It can be seen from the peak power comparisons which are shown in Fig. 2 and Fig. 3. When $\gamma(z)$ is considered, the powers and chirps are shown in Fig. 4. It can be seen that the powers and chirps under γ_{eff} and $\gamma(z)$ are very close, along with the maximum difference of 0.07 W and 9 THz in the cyan region. When the nonlinearity increases as z increases, the nonlinear effect becomes more and more severe. New frequency components will increase. As the effect of GVD is weakened, the broadening speed of newly generated frequency component is further reduced. The original frequency component has a slower reduction in the spreading speed than the newly generated frequency component. Finally, when the frequency component is sufficiently large, the middle portion of the pulse in the time domain will over-expand. The self-similar propagation of the PP will not be achieved. In the Case 2, the nonlinear effect is not enhanced so much that the effects of the nonlinear and GVD can maintain a balance. Therefore, for the Case 2, the self-similar propagation of the PP can be achieved in the silicon waveguide taper designed, and γ_{eff} used is valid.

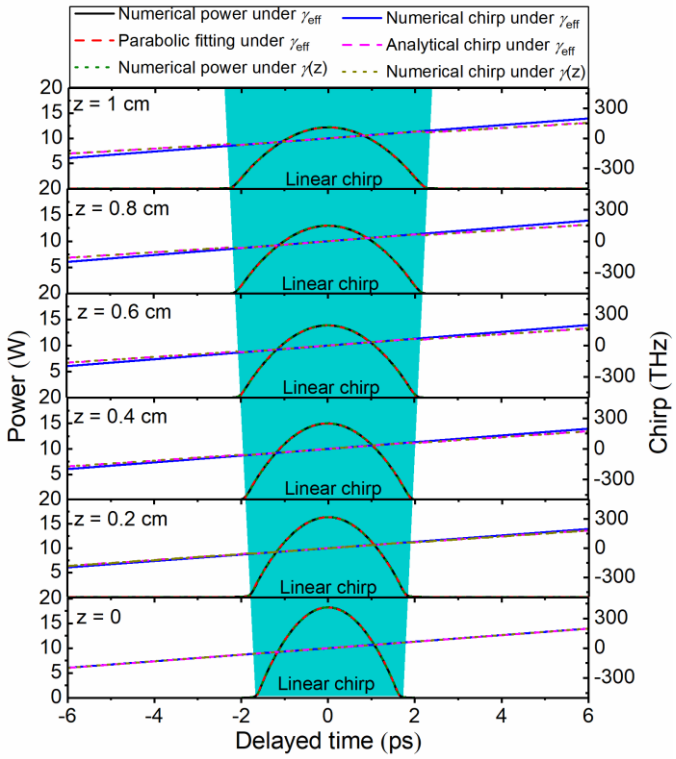

Fig. 4. The powers and chirps of the PP propagation in the designed silicon waveguide taper for the Case 2. Numerical powers (black solid curve) and chirps (blue solid curve), parabolic fittings (red dashed curve) and analytical chirps (pink dashed curve) under γ_{eff}, numerical powers (olive dot curve) and chirps (dark yellow dot curve) under γ(z) are shown at z = 0, 0.2, 0.4, 0.6, 0.8, and 1 cm, respectively. The cyan region corresponds to the region of the linear chirp.

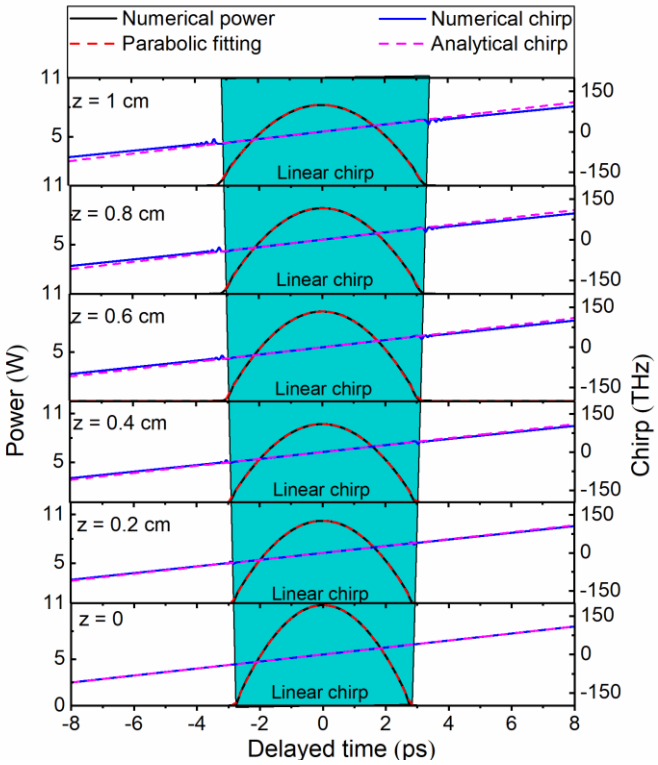

Fig. 5. The powers and chirps of the PP propagation in the designed silicon waveguide taper for the Case 3. Numerical powers (black solid curve), parabolic fittings (red dashed curve), numerical chirps (blue solid curve) and analytical chirps (pink dashed curve) are shown at z = 0, 0.2, 0.4, 0.6, 0.8, and 1 cm, respectively. The cyan region corresponds to the region of the linear chirp.

For the Case 1 and Case 2, although the self-similar propagation can be achieved, it is not easy to design such a taper whose $\gamma(z)$ or $\beta_2(z)$ is kept as a constant. Therefore, we consider the Case 3, where both $\gamma(z)$ and $\beta_2(z)$ are variable. Fig. 5 shows the propagation of the PP calculated for the Case 3. From Fig. 5, the pulse shape maintains parabola well from z = 0 to z = 1 cm. In this case, as z increases, the nonlinear coefficient increases, and the GVD coefficient reduces. For appropriate nonlinearity and GVD, the stretching profile of the new and original frequency components appears the parabolic distribution in the time domain. Thus, the self-similar propagation of the PP is achieved. It should be noted that the numerical and analytical chirps are not completely identical beyond the cyan region for the three cases considered. Chirp oscillations near the leading and trailing edges are observed and become larger as z increases. This means that not all pulse components obey the self-similar propagation. It has been proved that the pulse profile gradually becomes exponent at both edges during the propagation [13].

We will further analyze the evolutions of the peak power and full width at half maximum (FWHM) of the propagation pulse. The FWHM of the PP is about $1.414t_p$. The initial peak power and FWHM of the pulse for the three cases can be calculated from the analytical solutions. As shown in Fig. 6, the peak power of propagation pulse decreases, and the corresponding FWHM increases along z. The calculation results agree well with the analytical ones in which γ_{eff} and $\beta_{2,eff}$ are used, as shown in Figs. 6(a) and 6(b), respectively. In Fig. 6(c), the evolutions of the peak power and FWHM of the propagation pulse also match the analytical ones well. Thus, it can be concluded that the self-similar propagation of the PP can be achieved if the following two conditions are satisfied. (i) The initial peak power and FWHM of the propagation pulse are equal to the required value of the analytical solutions at z = 0. (ii) $\beta_2(z)$ and $\gamma(z)$ of the waveguide taper designed should satisfy the conditions of the self-similar propagation, which are given in Eqs. (13), (21), and (25). However, when we use $\gamma(z)$ instead of γ_{eff} in the calculation for the Case 1, small deviations of the peak power and FWHM are observed from Fig. 6(a). The maximum deviations of the peak power and FWHM are 0.13 W and 0.06 ps, respectively. For the Case 2, the deviations become smaller, as seen from Fig. 6(b). These results further indicate that the silicon waveguide tapers designed can support the self-similar propagation of the PP. Besides, there is no specific requirement for the profile of the input pulse. For example, if the input pulse has a Gaussian profile, it will gradually evolve to the PP and then propagate with a parabolic profile [2, 13, 28]. In the following, we will generate the PP with the silicon waveguide taper designed and then compress it in a cascaded silicon strip waveguide with anomalous dispersion profile.

III. The PP Compression In The Cascaded Silicon Waveguide

In Figs. 2, 3, and 4, the chirps of generated PP are linear, along with positive slopes. In this section, we will design three

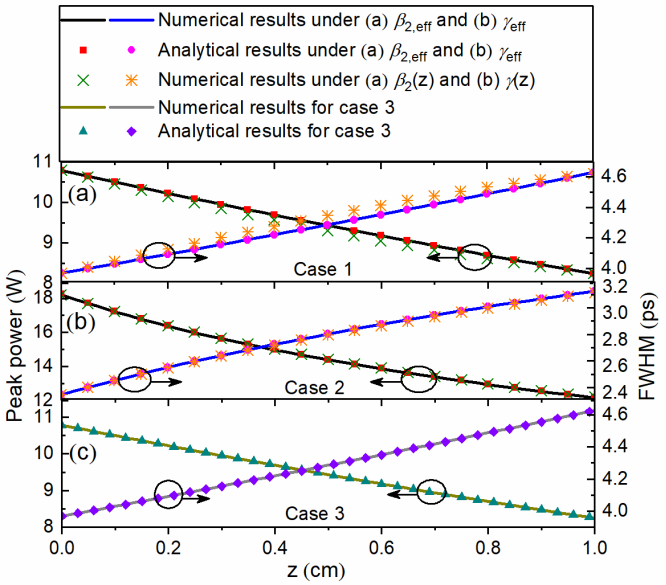

Fig. 6. (a) For the Case 1, numerical results of the peak power (black solid curve) and FWHM (blue solid curve) under $\beta_{2,eff}$, analytical results of the peak power (red square dot) and FWHM (pink circle dot) under $\beta_{2,eff}$, and numerical results of the peak power (olive cross) and FWHM (orange snowflake) under $\beta_2(z)$. (b) For the Case 2, numerical results of the peak power (black solid curve) and FWHM (blue solid curve) under γ_{eff}, analytical results of the peak power (red square dot) and FWHM (pink circle dot) under γ_{eff}, and numerical results of the peak power (olive cross) and FWHM (orange snowflake) under $\gamma(z)$. (c) For the Case 3, numerical results of the peak power (dark yellow curve) and FWHM (gray curve), and analytical results of the peak power (dark cyan triangle) and FWHM (violet diamond).

kinds of cascaded silicon waveguide in order to achieve the PP compression. Gaussian pulse without the initial chirp is chosen as the input pulse for the PP generation. In the simulation, $\beta_2(z)$ and $\gamma(z)$ are used for the three cases. The linear loss, nonlinear losses including TPA and TPA-induced free-carrier absorption (FCA), higher-order dispersion, and higher-order nonlinear effects including self-steepening and Raman effects are considered.

A. *Theoretical model of the pulse propagation*

The GINLSE is used to describe the nonlinear propagation in the silicon waveguide as following [29]

$$\frac{\partial A}{\partial t}=i\sum_{2}^{6}\frac{i^n\beta_n(z)}{n!}\frac{\partial^n A}{\partial t^n}+i\gamma(z)\left(1+\frac{i}{\omega_0}\frac{\partial}{\partial t}\right)A \times\int_{-\infty}^{t}R(t-t')\left|A(z,t')\right|^2dt'-\frac{1}{2}(\sigma_f+\sigma_l)A, \tag{31}$$

where $\beta_n(z)$ (n = 1, 2, 3,…6) is the n-th order dispersion coefficients at z. $\gamma(z)=2\pi n_2/[\lambda A_{eff}(z)]+i\beta_{TPA}/[2A_{eff}(z)]$, where $n_2 = 4.5\times10^{-18}$ m^2/W is the nonlinear refractive index, and $\beta_{TPA} = 4.5\times10^{-12}$ m/W is the TPA coefficient [30]. $R(t)=(1-f_R)\delta(t)+f_R h_R(t)$ is the nonlinear response function, where $h_R(t)$ is the Raman response function and $f_R = 0.043$ for the silicon material. The expression of $h_R(t)$ can be deduced from the Raman gain spectrum. $\sigma_f=\sigma(1+i\mu)N_c$ and σ_l = 0.5 dB/m are the nonlinear and linear losses, respectively, where $\sigma = 1.45\times10^{-21}$ m^2 is FCA coefficient, $\mu = 2k_c k_0/\sigma$ represents the free-carrier dispersion with $k_c = 1.35\times10^{-27}$ m^3, and N_c is the free-carrier density, which is determined by the rate equation [29]

$$\frac{\partial N_c(z,t)}{\partial t}=\frac{\beta_{TPA}}{2h\nu_0}\frac{\left|A(z,t)\right|^4}{A_{eff}^2}-\frac{N_c(z,t)}{\tau_{eff}}, \tag{32}$$

where τ_{eff} is the effective carrier lifetime depending on the geometrical structures of silicon waveguide. τ_{eff} is given as [31]

$$\frac{1}{\tau_{eff}}=\frac{1}{\tau_b}+\frac{S}{H}+2\sqrt{\frac{D}{W^2}\left(\frac{1}{\tau_b}+\frac{S+S_1}{H}\right)}, \tag{33}$$

where τ_b = 3 μs is the bulk recombination life time, $S = 8\times10^3$ cm/s is the interface recombination velocity, H is the height of waveguide, D = 16 cm^2/s is the diffusion coefficient, W is the width of waveguide, and $S_1 = S$ is the surface recombination velocity. τ_{eff} will change as W varies with z.

B. *Design of the cascaded silicon waveguide*

The cascaded silicon waveguide designed for each case is divided into three segments, which are named as Segments A, B, and C. Segment A is designed according to the condition of self-similar propagation demonstrated in section II. It is used for the PP generation from the initial Gaussian input pulse without chirp. Segment B is a short silicon waveguide taper where the normal GVD is transferred to the anomalous GVD. For Segment C, a strip silicon waveguide is designed for the PP compression. The 3D sketch of the proposed cascaded silicon waveguide is shown in Fig. 6. W_1, W_2, and W_3 are the waveguide widths at the input port of Segment A (A_{in}), output port of Segment A (A_{out}), and output port of Segment C (C_{out}), respectively. L_1, L_2, and L_3 are the waveguide lengths of Segment A, Segment B, and Segment C. An input Gaussian pulse is described as

$$A(0,t)=\sqrt{P_0}\exp\left(-t^2/\left(2T_0^2\right)\right), \tag{34}$$

where P_0 = 2.2 W is the peak power and T_0 is the initial pulse width. $T_F = 1.665T_0$ is the FWHM and set as 300 fs. The mode field profiles of the propagation pulse at the input and output ports of the cascaded silicon waveguide at wavelength 1550 nm are shown in Fig. 7. It can be seen that the mode fields can be well confined in the waveguide. The values of L_1, W_1, and W_2 are 1 cm, 1600 nm, and 800 nm, respectively. For Segment A, the geometrical parameters are the same as the proposed silicon waveguide tapers in section II. In Figs. 8(a), 8(b), and 8(c), the profiles and chirps of the output pulses from Segment A for the three cases are fitted by the parabolic curves and straight lines, respectively. Good agreements can be seen except for the deformation at the leading and trailing edges.

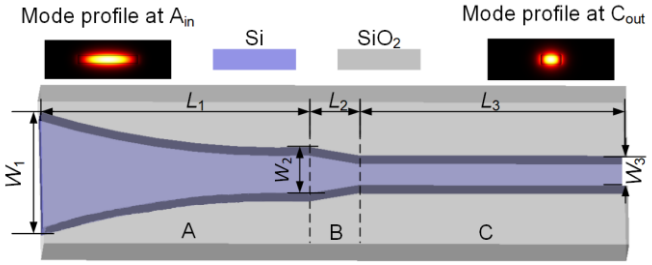

Fig. 7. The 3D sketch of the cascaded silicon waveguide proposed for the generation and compression of the PP. The mode field profiles at the input port of Segment A and output port of Segment C are also shown when wavelength is located at 1550 nm.

To quantitatively evaluate the difference between the output pulse and PP, a mismatched parameter δ is defined as

$$\delta^2 = \frac{\int_{-\infty}^{+\infty}\left[P(t)-P_f(t)\right]^2 dt}{\int_{-\infty}^{+\infty}P^2(t)\,dt}, \tag{35}$$

where $P(t)$ and P_f are the powers of the output pulse and parabolic fitting. As shown in Fig. 8(d), for the three cases, δ gradually decreases along z, and the Gaussian pulses evolve to the PP. It can be also seen from Figs. 8(a), 8(b), and 8(c) that the output chirps are linear, along with a positive slope. In order to

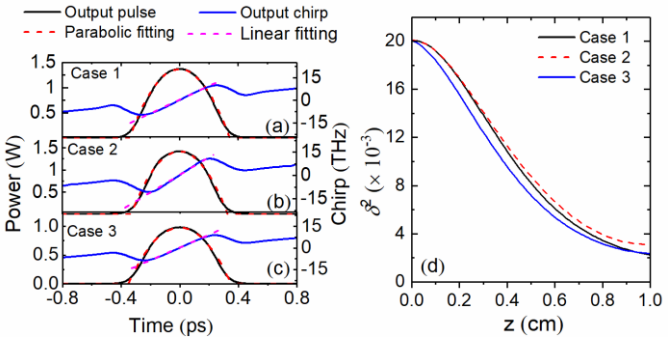

Fig. 8. The profiles of the output pulse (black solid curve), parabolic fitting (red dashed curve), output chirp (blue solid curve), and linear fitting (pink dashed curve) from Segment A for (a) Case 1, (b) Case 2, and (c) Case 3. (d) The mismatched parameters for Case 1 (black solid curve), Case 2 (red dashed curve), and Case 3 (blue solid curve).

achieve the PP compression, a transitional silicon waveguide taper, namely Segment B, needs to be designed. L_2 and W_3 are chosen as 20 μm and 545 nm, respectively. From the input to output ports of Segment B , β_2 changes from 5.53×10^{-25} to -5.13×10^{-25} ps^2/m. Since the effective mode area A_{eff} reduces along z, γ increases from 136.71 to 165.67 W^{-1}m^{-1}. Segment C is a strip silicon waveguide, whose β_2 and γ are -5.13×10^{-25} ps^2/m and 165.67 W^{-1}m^{-1}, respectively. To completely compensate the chirp generated in Segment A, L_3 are chosen as 2.06, 1.77, and 2.35 cm for the Case 1, Case 2, and Case 3, respectively. L_3 are different because the propagation pulses have different self-similar evolutions before entering Segment C. All geometrical parameters of the cascaded silicon waveguide are summarized in Table I.

TABLE I
GEOMETRICAL PARAMETERS OF CASCADED SILICON WAVEGUIDE

	Unit: cm			Unit: nm		
Case	L_1	L_2	L_3	W_1	W_2	W_3
1	1	0.002	2.06	1600	800	545
2	1	0.002	1.77	1600	800	545
3	1	0.002	2.35	1600	800	545

C. Simulation results and discussion

For the Case 1, Case 2, and Case 3, the total lengths of the cascaded silicon waveguides are chosen as 3.062, 2.772, and 3.352 cm, respectively. The corresponding evolutions of the temporal pulses along z are shown in Figs. 9(a), 9(b), and 9(c), respectively, where the insets show the pulse propagation dynamics in Segment B. From Figs. 9(a), 9(b), 9(c), and the insets, the input Gaussian pulse experiences three evolution

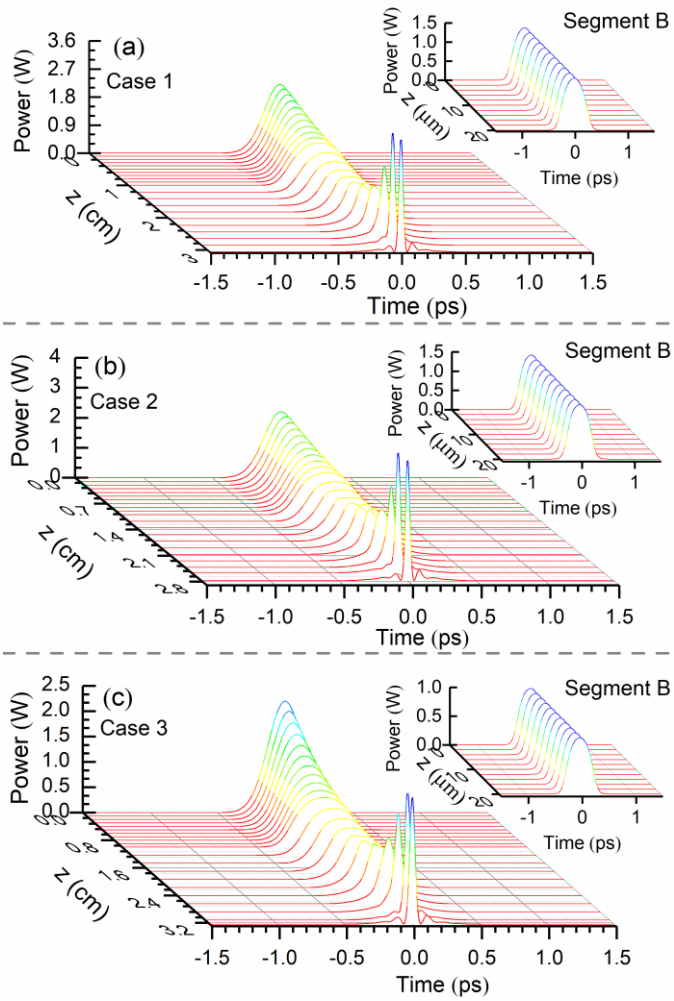

Fig. 9. The evolutions of the temporal pulses in the cascaded silicon waveguide for (a) Case 1, (b) Case 2, and (c) Case 3. The insets in (a), (b), and (c) are the evolutions of the temporal pulses in Segment B.

stages. First, it gradually evolves to the PP in Segment A, accompanying with the pulse broadening and peak power decreasing. Then, the PP is propagated in Segment B without any change. Finally, the PP is quickly compressed in Segment C. Small pedestals of the output pulse can be observed at the leading and trailing edges. The main reasons are considered as following. The chirps with the positive slopes generated in Segment A and Segment C are not linear at the leading and trailing edges. They cannot be completely compensated by the linear chirp with a negative slope generated by the GVD in Segment C.

The FWHMs and peak powers at the input and output ports of each segment are summarized in the Table II for comparison. It can be seen that the FWHM and peak power at A_{out} are different in the three cases even if the input is the same at A_{in}. For the Case 3, it has the largest FWHM and smallest peak power. Furthermore, after the PP compression, the FWHM and peak power at C_{out} are also different. The compression ratio, which is defined as the ratio of FWHM between the input and output ports of cascaded silicon waveguide, are 7.98, 8.43, and 6.54 for the Case 1, Case 2, and Case 3, respectively. From Fig. 8(d) and Table II, good self-similar evolution does not necessarily lead to large compression ratio.

TABLE II
PULSE PARAMETERS AT EACH PORT

	FWHM (fs)			Peak power (W)		
Case	A_{in}	A_{out}	C_{out}	A_{in}	A_{out}	C_{out}
1	300	464.9	37.6	2.2	1.37	3.61
2	300	443.7	35.6	2.2	1.42	4.01
3	300	475.5	45.9	2.2	0.98	2.49

In order to clearly demonstrate the process of the PP compression in the cascaded silicon waveguide, the variations of the FWHM, peak power, and chirp slope along z in each segment are shown in Fig. 10. The horizontal axes in Fig. 10 represent the propagation distance. Each segment of the cascaded waveguide is shown separately on the horizontal axis so as to make the variation of the pulse parameters more clearly. Here, we take the Case 1 as an example. In Fig. 10(a), the FWHM increases from 300 to 464.9 fs, the corresponding peak power decreases from 2.2 to 1.37 W, and the chirp slope increases from 0 to 49.5 THz^2 in Segment A. This process corresponds to the PP generation. In a passive and tapered waveguide, the PP generation is always accompanied by the increase of the pulse width, decrease of the peak power, and formation of a chirp with positive slope. But they remain almost unchanged in Segment B because L_2 is so short that the interaction between the GVD and nonlinearity can be neglected. In contrast, the FWHM is reduced to 37.6 fs, the peak power is increased from 1.37 to 3.61 W, and the chirp slope is decreased from 49.5 to −215 THz^2 in Segment C. It is noted that the variation of the peak power in Segment C includes three stages. First, the peak power decreases from 1.37 to 1.11 W as z changes from 0 to 1.07 cm. Then, it rapidly increases from 1.11 to 3.9 W as z changes from 1.07 to 1.96 cm. Finally, it decreases from 3.9 to 3.61 W as z changes from 1.96 to 2.06 cm. The nonlinear interaction in the three stages can be characterized as follows. When $0 < z < 1.07$ cm, the chirp with a positive slope generated in Segment A is compensated by the chirp with a negative slope generated in Segment C, so the FWHM is reduced. However, the peak power is also reduced because the effects of the anomalous GVD and losses are stronger. Due to the nonlinear effect, the chirp slope has a slight increase. When the pulse propagates from 1.07 to 1.96 cm, because large chirp with a positive slope induced by the nonlinearity cannot be completely compensated by the chirp with a negative slop caused by the anomalous GVD, the PP compression occurs, along with the increase of the peak power. However, as z increases, the chirp slope decreases slightly, then increases sharply and decreases rapidly until the end of the waveguide. The slight decrease in the chirp slope is due to the very low peak power at 1.07 cm and the weakening of the nonlinear effect. After that, the chirp slope is greatly increased, which is resulted from the rapid increase of the peak power. The position where the chirp slope begins to fall is not the same as the position where the peak power begins to decrease, but it is consistent with the position where the FWHM is constant. The main reason for this phenomenon is considered that the effect of dispersion is gradually enhanced and ultimately stronger than the nonlinear effect as the pulse width decreases. With the increase of the peak power, the nonlinear loss also increases rapidly. Consequently, when $1.96 < z < 2.06$ cm, the nonlinear loss reduces the peak power and weakens the interaction between the nonlinearity and GVD. When $z > 1.96$ cm, the FWHM is almost unchanged, as shown in Fig. 10(a). This is because the chirp with a positive slope is completely compensated by the chirp with a negative slope. The evolutions of the FWHM and peak power for the Cases 2 and Case 3 in Figs. 10(b) and 10(c) show the similar behavior with that in Fig. 10(a) except for the details in each segment. This can be attributed to the fact that for Segment A in the three cases, the evolution degree from the Gaussian pulse to the PP is different.

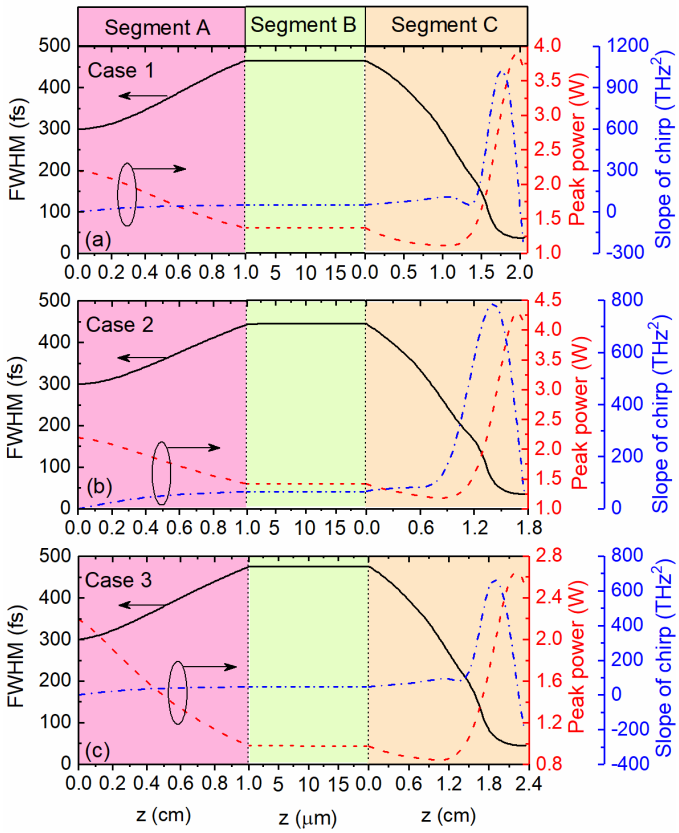

Fig. 10. The evolutions of the pulse widths (red solid curves), peak powers (blue dashed curves) and slope of chirp (blue dashed dot curves) versus z in each segment for (a) Case 1, (b) Case 2, and (c) Case 3.

IV. Conclusions

In summary, the conditions of the self-similar propagation of the PP in passive nonlinear tapers are derived and classified into the three cases. Three kinds of silicon waveguide tapers are then designed to numerically verify the conditions. Simulation results show that the self-similar propagation of the PP can be realized. Cascaded silicon waveguides based on the silicon waveguide tapers is further designed to generate and compress the PP. It is demonstrated that the PP can be generated and compressed to 35.6 fs, which is nearly chirp-free and has small pedestals. We believe that the proposed scheme of the PP generation and compression can find important applications in the on-chip integrated all-optical signal processing and ultrafast imaging system.

REFERENCES

[1] D. Anderson, M. Desaix, M. Karlsson M. Lisak, and M. L. Quiroga-Teixeiro, "Wave-breaking-free pulses in nonlinear-optical fibers," *Opt. Lett.*, vol. 10, no. 7, pp. 1185-1190, Jul. 1993.

[2] M. E. Fermann, V. I. Kruglov, B. C. Thomsen, J. M. Dudley, and J. D. Harvey, "Self-Similar Propagation and Amplification of Parabolic Pulses in Optical Fibers," *Phys. Rev. Lett*., vol. 84, no. 26, pp. 6010-6013, Jun. 2000.

[3] J. Limpert, T. Schreiber, T. Clausnitzer, K. Zöllner, H.-J. Fuchs, E.-B. Kley, and H. Zellmer, "High-power femtosecond Yb-doped fiber amplifier," *Opt. Express*, vol. 10, no. 14, pp. 628-638, Jul. 2002.

[4] T. Schreiber, C. K. Nielsen, B. Ortac and J. Limpert, A. Tünnermann "Microjoule-level all-polarization-maintaining femtosecond fiber source," *Opt. Lett*., vol. 31, no. 5, pp. 574-576. Mar. 2006.

[5] P. Dupriez *et al*., "High-power, high repetition rate picosecond and femtosecond sources based on Yb-doped fiber amplification of VECSELs," *Opt. Express*, vol. 14, no. 21, pp. 9611-9616, Jul. 2006.

[6] F. Parmigiani, P. Petropoulos, M. Ibsen, and D. J. Richardson, "Pulse Retiming Based on XPM Using Parabolic Pulses Formed in a Fiber Bragg Grating," *IEEE Photon. Technol. Lett*., vol. 18, no. 7, pp. 829-831, Apr. 2006.

[7] C. Finot and G. Millot, "Synthesis of optical pulses by use of similaritons," *Opt. Express*. Vol. 12, no. 21, pp. 5104-5109, Oct. 2004.

[8] T. Hirooka, and M. Nakazawa, "All-Optical 40-GHz Time-Domain Fourier Transformation Using XPM With a Dark Parabolic Pulse," *IEEE Photon. Technol. Lett*., vol. 20, no. 22, pp. 1869-1871, Nov. 2008.

[9] C. Finot, S. Pitois and G. Millot, "Regenerative 40 Gbit/s wavelength converter based on similariton generation," *Opt. Lett*., vol. 30, no. 14, pp. 1776-1778, Jul. 2005.

[10] T. T. Ng, F. Parmigiani, M. I., Z. Zhang, P. Petropoulos, and D. J. Richardson, "Compensation of Linear Distortions by Using XPM With Parabolic Pulses as a Time Lens," *IEEE Photon. Technol. Lett*., vol. 20, no. 13, pp. 1097-1099, Apr. 2006.

[11] T. Hirooka, and M. Nakazawa, "Parabolic pulse generation by use of a dispersion-decreasing fiber with normal group-velocity dispersion," *Opt. Lett*., vol. 29, no. 5, pp. 498-500, Mar. 2004.

[12] S. Lavdas, J. B. Driscoll, H. Jiang, R. R. Grote, R. M. Osgood, Jr., and N. C. Panoiu, "Generation of parabolic similaritons in tapered silicon photonic wires: comparison of pulse dynamics at telecom and mid-infrared wavelengths," *Opt. Lett.*, vol. 38, no. 19, pp. 3953-3956, Oct. 2013.

[13] V. I. Kruglov, and J. D. Harvey, "Asymptotically exact parabolic solutions of the generalized nonlinear Schrödinger equation with varying parameters," *J. Opt. Soc. Am. B*, vol. 23, no. 12, pp. 2541-2550, Dec. 2006.

[14] K. C. Chan, S. Memer, and H. F. Liu, "Short Pulse Generation by Higher Order Soliton-Effect Compression: Effects of Optical Fiber Characteristics," *IEEE J. Quan. Electron.*, vol. 31, no.12, pp. 2226-2235, Dec. 1995.

[15] D. T. H. Tan, A. M. Agarwal, and L. C. Kimerling, "Nonlinear photonic waveguides for on-chip optical pulse compression," *Laser Photonics Rev*., vol. 9, no. 3, pp. 294-308, Apr. 2015.

[16] L. F. Mollenauer, R. H. Stolen, and J. P. Gordon, and W. J. Tomlinson, "Extreme picosecond pulse narrowing by means of soliton effect in single-mode optical fibers," *Opt. Lett.*, vol. 8, no. 5, pp. 289-291, May. 1983.

[17] S. Lavdas, J. B. Driscoll, R. R. Grote, R. M. Osgood, Jr., and N. C. Panoiu, "Pulse compression in adiabatically tapered silicon photonic wires," *Opt. Express*, vol. 22, no. 6, pp. 6296-6312, Mar. 2014.

[18] A. C. Peacock, "Mid-IR soliton compression in silicon optical fibers and fiber tapers," *Opt. Lett.*, vol. 37, no. 5, pp. 818-820, Mar. 2012.

[19] C. Mei *et al*., "High Degree Picosecond Pulse Compression in Chalcogenide-Silicon Slot Waveguide Taper," *J. Lightw. Technol*., vol. 34, no. 16, pp. 3843-3852, Aug. 2016.

[20] A. B. Redondo, C. Husko, D. Eades, Y. Zhang, J. Li, T.F. Krauss, and B.J. Eggleton, "Observation of soliton compression in silicon photonic crystals," *Nat. Commun.*, vol. 5, no.3160, pp. 1-8, Jan. 2014.

[21] P. Colman, C. Husko, S. Combrie, I. Sagnes, C. W. Wong, and A. De Rossi1, "Temporal solitons and pulse compression in photonic crystal waveguides," *Nat. Photon*., vol. 4, pp. 862-868. Dec. 2010.

[22] W. J. Tomlinson, R.H. Stolen, and C. V. Shank, "Compression of optical pulses chirped by self-phase modulation in fibers," *J. Opt. Soc. Am. B*, vol. 1, no. 2, pp. 139-149, Apr. 1984.

[23] D. Krčmařík, R. Slavík, Y. Park, and J. Azaña, "Nonlinear pulse compression of picosecond parabolic-like pulses synthesized with a long period fiber grating filter," *Opt. Express*. vol. 17, no. 9, pp. 7074-7087, Apr. 2009.

[24] Z.Y. Huang, Y. X. Leng, and Y. Dai, "Femtosecond parabolic pulse nonlinear compression with gas-filled hollow-core fiber," *Chin. Phys. B*, vol. 23, no. 12, pp. 124210-1-5, Oct. 2014.

[25] D. T. H. Tan, P. C. Sun, and Y. Fainman, "Monolithic nonlinear pulse compressor on a silicon chip," *Nat. Commun*., vol. 1, pp, 1-6, Nov. 2010.

[26] M. Peccianti *et al*., "Subpicosecond optical pulse compression via an integrated nonlinear chirper," *Opt. Express*. vol. 18, no. 8, pp. 7625-7633, Apr. 2010.

[27] V. I. Kruglov, A. C. Peacock, and J. D. Harvey, "Self-similar propagation of parabolic pulses in normal-dispersion fiber amplifiers," *J. Opt. Soc. Am. B*, vol. 19, no. 3, pp. 461-469, Mar. 2002.

[28] C. Mei *et al*., "Comprehensive analysis of passive generation of parabolic similaritons in tapered hydrogenated amorphous silicon photonic wires," *Sci. Rep.*, vol. 7, no. 1, pp. 3814-1-14, Jun. 2017.

[29] A. Peacock, and N. Healy, "Parabolic pulse generation in tapered silicon fibers," *Opt. Lett.*, vol. 35, no. 11, pp. 1780-1782, Jun. 2010.

[30] H. K. Tsang, C. S. Wong, T. K. Liang, I. E. Day, S. W. Roberts, A. Harpin, J. Drake, and M. Asghari, "Optical dispersion, two-photon absorption and self-phase modulation in silicon waveguides at wavelength," *Appl. Phys. Lett*., vol. 80, no. 3, pp. 416-418, Jan. 2002.

[31] D. Dimitropoulos, R. Jhaveri, R. Claps, J. C. S. Woo, and B. Jalali, "Lifetime of photogenerated carriers in silicon-on-insulator rib waveguides," *Appl. Phys. Lett*., vol. 86, pp. 071115-1-3, Feb. 2005.